ACADEMIC PRESS

Available online at www.sciencedirect.com

SCIENCE DIRECT®

Journal of Sound and Vibration 271 (2004) 883–904

JOURNAL OF SOUND AND VIBRATION

www.elsevier.com/locate/jsvi

Contribution to experimental validation of linear and non-linear dynamic models for representing rotor–blade parametric coupled vibrations

I.F. Santos[a,*], C.M. Saracho[b], J.T. Smith[a], J. Eiland[a]

[a] *MEK - Department of Mechanical Engineering, DTU - Technical University of Denmark, Lyngby 2800, Denmark*
[b] *FEM/DPM, Department of Mechanical Design, UNICAMP, State University of Campinas, Campinas, Brazil*

Received 2 September 2002; accepted 12 March 2003

Abstract

This work makes a theoretical and experimental contribution to the problem of rotor–blades dynamic interaction. A validation procedure of mathematical models is carried out with the help of a simple test rig, built by a mass–spring system attached to four flexible rotating blades. With this test rig, it is possible to highlight some dynamic effects and experimentally simulate the structural behaviour of a windmill in two dimensions (2-D model). Only lateral displacement of the rotor in the horizontal direction is taken into account. Gyroscopic effect due to angular vibrations of the rotor is eliminated in the test rig by attaching the rigid rotor to a flexible foundation. The blades are modelled as Euler–Bernoulli beams. Using three different approaches to describe the beam deformation one achieves: (a) a linear model; (b) a linear beam model with second order terms; (c) a fully non-linear model. Tip masses at the end of the blades emphasize the coupling between the dynamic and elastic terms. The shape functions are chosen in order to reduce the mathematical model, so that only the first bending mode of the beam is taken into account. The resulting equations of motion have five degrees of freedom and illustrate linear, non-linear and time-dependent terms in a very transparent way. Although neither gyroscopic effect due to rotor angular vibrations nor higher blade mode shapes are considered in the analysis, the equations of motion of the rotor–blades system are still general enough for the purpose of the work: validation of different linear and non-linear models with time dependent (periodic) coefficients. Experiments are carried out in the time and frequency domains while the rotor operates with different constant angular velocities.
© 2003 Elsevier Ltd. All rights reserved.

*Corresponding author. Tel.: +45-4525-6269; fax: +45-4588-1451.
E-mail address: ifs@mek.dtu.dk (I.F. Santos).

0022-460X/$ - see front matter © 2003 Elsevier Ltd. All rights reserved.
doi:10.1016/S0022-460X(03)00758-2

1. Introduction

The main change detected in the dynamic behaviour of a rotating beam is the increase of the natural frequencies with the rotation speed, an effect known as centrifugal stiffening. This effect is only correctly described by a mathematical model if non-linear terms related to the beam deformation are taken into account [1]. At least a second order linearization scheme of the deformation vector must be employed to ensure that the effect of centrifugal stiffening is appropriately taken into account, once those non-linear terms are responsible for transferring part of rotation energy to the bending motion [2]. The application of such a linearization of second order introduces a matrix of geometric stiffness, due to the terms of centrifugal stiffening. When the blades are subjected to constant rotational speeds, this matrix may be calculated either from the solution of the initial stress problem or from the normal force acting on the blade [3]. However, in the most general case, this matrix is not constant, as it depends on the longitudinal displacements of the beam [4]. The influence of the derivative of the geometric stiffness matrix and other higher order non-linear terms, which are usually neglected, can sometimes lead to different solutions [5]. However, after including those high order non-linear terms in the formulation, the solution becomes extremely sensitive to the shape function used for modelling the axial displacement. Thus, it is necessary to include a large number of axial modes to correctly model the interaction between the axial and transverse motion, otherwise the numerical solution becomes unstable. Mayo et al. [6] discuss the numerical efficiency of the non-linear model for modelling rotating beams. Another approach to this problem is to assume that the axial displacements originate from transverse deformation without axial deformation. This approach leads to a more efficient and stable numerical model. Moreover, it is not necessary to include any axial mode, depending upon the range of frequencies. This kind of formulation, in which the displacement and the axial deformation are uncoupled, is valid only for systems whose axial stiffness is much higher than the transverse one, for example in windmills. Therefore, the correct choice of the beam model is essential to ensure that coupling between elastic deformation and rotational motions is properly taken into account [2].

The equations of motion for a single cantilever beam, parametrically excited, is presented by Cartmell [7,8] using Lagrange's formulation. The intention of that work [7] was to illustrate the use of classical engineering theories in the accurate modelling of a very simple structure, and to highlight the conceptualization of such a three-dimensional problem. In this work, the equations of motion of four rotating cantilever beams, attached to tip masses and to a mass–spring system, are obtained using the Newton–Euler–Jourdain Method [9]. This two-dimensional model is employed to analyze how the lateral vibrations of the mass–spring system (non-rotating parts of a structure) influence the bending vibrations of the blades (rotating parts) and vice versa. The blade (beam) deformations are obtained using three different approaches: (a) only small displacements are assumed, leading to a linear deformation vector and thus to a linear model of the whole assembly; (b) large displacements are included, but to obtain the deformation vector only the non-linear terms of the second order are considered, resulting in linear equations, with a new matrix due to the geometric stiffness; (c) a fully non-linear model for the deformation of the beam. Experimental and numerical results obtained with these three different models are presented, clarifying their limitations and the range of application.

2. Test facilities

The test rig for validating these three different mathematical models is presented in Fig. 1(a) and described as follows:

- A rotating disc (disc + motor) is fixed rigidly to a foundation. The disc–motor–foundation builds a single concentrated mass, and is connected to the inertial frame by means of four flexible beams with adjustable length, i.e. adjustable springs. This arrangement allows only linear motion of the rotor centre and eliminates the gyroscopic effects due to angular motion of

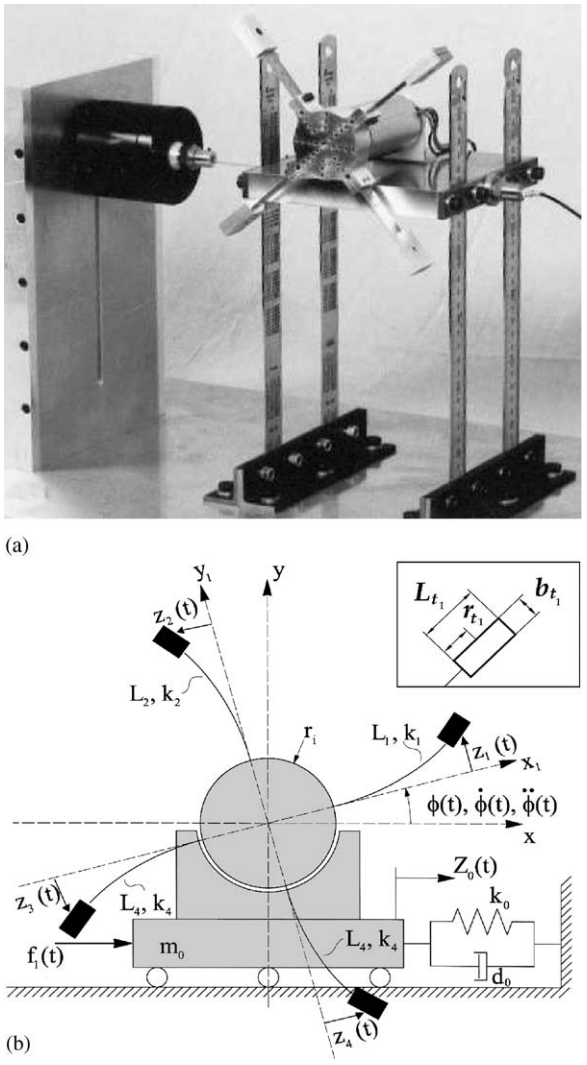

Fig. 1. (a) Test rig built by: rotor-foundation supported by flexible beams; four flexible rotating beam with tip masses attached to their ends; electromagnetic shaker attached to foundation by means of a wire; and acceleration sensors fixed to foundation. (b) Mechanical model illustrating: reference frames I and B_1; degrees of freedom $z_o(t)$, $z_1(t)$, $z_2(t)$, $z_3(t)$, $z_4(t)$; and main reference points O and O_i $(i = 1, \ldots, 4)$.

the rotor–foundation. Thus, the mass–spring system has only one degree of freedom, i.e. linear displacement in the horizontal direction.

- Four masses (particles) are connected to the rotating disc by means of flexible beams (blades) with adjustable length. The movements of the tip masses are described by linear displacements in the rotating reference frame. Only the first beam bending mode is of importance in the defined range of frequencies.
- An electromagnetic shaker is used to excite the mass–spring system in the horizontal direction. An acceleration sensor is used to measure the linear movements of the mass–spring system and indirectly detect changes of the blade dynamic behaviour.
- The test rig damping, specifically the damping factor related to the blade mode shapes, is kept extremely small. This facilitates the measurements while capturing the blades' vibrations by means of an acceleration sensor attached to the non-rotating part of the test rig.

The tip mass considerably influences the dynamic response of the beam, once it strengthens the coupling between the dynamic terms and elastic ones [10,11]. The restriction of the motion in the vertical plane allows theoretical as well as experimental analyses to be carried out with a 2-D model in the frequency range of 0–50 Hz.

3. Mathematical model of rotor–blades assembly

The mechanical model for representing the test rig is illustrated in Fig. 1(b). The model parameters are shown in Table 1. The associate mathematical model has five degrees of freedom, $\mathbf{q}(t) = \{z_o(t)\ z_1(t)\ z_2(t)\ z_3(t)\ z_4(t)\}^{\mathrm{T}}$, where the first co-ordinate, z_o describes the horizontal motion of the mass–spring system, and the other four, z_i $(i = 1, 2, 3, 4)$, represent the displacement of the tip masses p_i relative to the rotating co-ordinate system $B_1(x_1, y_1)$. The co-ordinate system B_1 rotates with angular speed $\dot{\phi}$.

The displacement and velocity of each blade are described using a shadow reference frame B_{p_i} (x_{p_i}, y_{p_i}). This shadow system rotates with the same angular speed $\dot{\phi}$ of the frame B_1, but with a constant phase of θ_i from the x_1-axis. The angles θ_i are related to the distribution of the beams

Table 1
Main parameters of the test rig

Mass–spring system		Flexible rotating beams $(i = 1, 2, 3, 4)$	
		θ_i	$(i-1)\pi/2$ rad
m_0	2.228 kg	m_i	0.0482 kg
r_0	0.040 m	r_i	0.040 m
L_0	0.200 m	L_i	0.046 m
b_0	0.025 m	b_i	0.015 m
h_0	0.001 m	h_i	0.0005 m
E	2.1e + 11 N/m^2	E_i	2.1e^{11} N/m^2
I_0	2.0833e − 12 m^4	I_i	1.5625e − 13 m^4
k_0	2.625 N/m;	k_i	384.5 N/m
ϵ	2e − 6 m	rt_i	0.015 m
		It_i	4.0167e − 6 kg m^2

around the rotor periphery. Such a reference frame simplifies the description of the beam deformation field. Using this system the absolute velocity of each blade p_i is given by

$$ {}_{B_{p_i}}\mathbf{v}_{p_i} = {}_{B_{p_i}}\mathbf{v}_{O_i} + {}_{B_{p_i}}\boldsymbol{\omega}_{B_{p_i}} \times ({}_{B_{p_i}}\mathbf{L}_i + {}_{B_{p_i}}\mathbf{u}_i) + \frac{\mathrm{d}}{\mathrm{d}t}({}_{B_{p_i}}\mathbf{u}_i), \tag{1} $$

where $\mathbf{v}_{O_i}$ is the velocity vector of point O_i, which the blade is fixed to, $\boldsymbol{\omega}_{B_{p_i}}$ is the angular velocity of the shadow system B_{p_i}. The position of the non-deformed blade-tip mass is given by $\mathbf{L}_i$, a vector from the clamping point O_i to the beam tip, and its displacement due to flexibility is written as $\mathbf{u}_i$.

The blades are modelled as Euler–Bernoulli beams with a tip mass attached to their free end. Neither shear force nor rotatory inertia, nor distributed mass of the beam, are taken into account. However, the finite dimensions of the tip mass cannot be neglected, as can be seen in Fig. 1(b). In this case, both mass m_i and rotatory inertia It_i must be included in the formulation. Moreover, the distance from the gravity centre of the tip mass to its clamping at the beam rt_i shall also be included.

The beam displacement is interpolated using a cubic polynomial, satisfying essential conditions, which are the clamping to the rotor at the point O_i. This shape function is chosen aiming at minimizing the number of degrees of freedom of the model. Such a function approximates only the first bending mode of the beam. According to that, the elastic displacement of the beam is given by

$$ {}_{B_{p_i}}\mathbf{u}_i = \begin{Bmatrix} 0 \\ v_i(\xi_i) \\ 0 \end{Bmatrix} = \begin{Bmatrix} 0 \\ \psi_i(\xi_i) z_i(t) \\ 0 \end{Bmatrix} \quad \text{where } \psi_i(\xi_i) = \frac{3}{2}\left(\frac{\xi_i}{L_i}\right)^2 - \frac{1}{2}\left(\frac{\xi_i}{L_i}\right)^3. \tag{2} $$

The rotatory inertia of the tip is taken into account assuming that the derivative of the tip displacement is equal to its angular motion (no shear force). Using this approach an equivalent mass is estimated so that the effects of rotatory inertia are included on the mathematical model. This equivalent mass is given by

$$ \bar{m}_i = m_i \psi(L_i)^2 + (It_i + m_i r t_i^2)\psi'(L_i)^2 + 2 m_i r t_i \psi(L_i)\psi'(L_i). \tag{3} $$

The equations of motion of the rotor–blades assembly are obtained using the Newton–Euler–Jourdain's equation [12]. The mass–spring potential energy π_o corresponds to the energy stored in the long beams of the foundation, while π_{l_i} to the potential energy due to the blade bending deformation. The energy π_{l_i} is obtained using linear approach (no longitudinal displacements). The term π_{g_i} is related to the blade geometrical stiffness. The three terms are

$$ \pi_o = \frac{1}{2} k_o z_o^2; \tag{4a} $$

$$ \pi_{l_i} = \frac{1}{2}\int_0^{L_i} EI\left(\frac{\partial^2 v_i}{\partial \xi_i^2}\right)^2 \mathrm{d}\xi_i = \frac{1}{2} k_i z_i^2 \quad \text{where } k_i = \frac{3EI}{L_i^3}; \tag{4b} $$

$$ \pi_{g_i} = \frac{1}{2}\int_0^{L_i} N_{p_i}(\xi_i)\left(\frac{\partial v_i}{\partial \xi_i}\right)^2 \mathrm{d}\xi_i, \tag{4c} $$

where $N_{p_i}(\xi_i)$ is the normal force, due to centrifugal acceleration, acting on the blade p_i.

In the *linear model* only the terms π_0 and π_{l_i} are taken into account. The inclusion of π_{g_i} means taking into account the second non-linear terms of the deformation vector, leading to *second order linearized model*. The *fully non-linear model* is obtained assuming that there is a longitudinal displacement resulting from a large transversal beam displacement. No axial deformation is taken into account and only the terms π_0 and π_{l_i} are included in this model, so that the non-linear terms of the deformation vector are implicitly considered [6,13]. In this case, the elastic displacement is given by

$$ {}_{B_{p_i}}\mathbf{u}_i = \begin{Bmatrix} u_i(\xi_i) \\ v_i(\xi_i) \\ 0 \end{Bmatrix} = \begin{Bmatrix} u_i(\xi_i) \\ \psi_i(\xi_i) z_i(t) \\ 0 \end{Bmatrix}, \quad \text{where } u_i = -\frac{1}{2}\int_0^{\xi_i} \left(\frac{\partial v_i}{\partial \xi}\right)^2 \mathrm{d}\xi. \tag{5} $$

The equations of motion for the three models, considering a rotor eccentricity ϵ, are:

- *Linear model*

$$ \mathbf{M}_0\ddot{\mathbf{q}} + \mathbf{C}\dot{\mathbf{q}} + (\mathbf{K}_0 + \mathbf{K}_1 + \mathbf{K}_2 + \mathbf{K}_{p_1})\mathbf{q} = \mathbf{f}_1 + \mathbf{f}_2 + \mathbf{f}_p. \tag{6a} $$

- *Second-order linearized model*

$$ \mathbf{M}_0\ddot{\mathbf{q}} + \mathbf{C}\dot{\mathbf{q}} + (\mathbf{K}_0 + \mathbf{K}_1 + \mathbf{K}_2 + \mathbf{K}_3 + \mathbf{K}_{p_1})\mathbf{q} = \mathbf{f}_1 + \mathbf{f}_2 + \mathbf{f}_p. \tag{6b} $$

- *Fully non-linear model*

$$ \begin{aligned} &(\mathbf{M}_0 + \mathbf{M}_1 + \mathbf{M}_2)\ddot{\mathbf{q}} + \mathbf{C}\dot{\mathbf{q}} + (\mathbf{K}_0 + \mathbf{K}_1 + \mathbf{K}_2 + \mathbf{K}_3 + \mathbf{K}_{p_1} + \mathbf{K}_{p_2})\mathbf{q} \\ &\quad = \mathbf{f}_1 + \mathbf{f}_2 + \mathbf{f}_p + \mathbf{s}_0 + \mathbf{s}_1 + \mathbf{s}_2 + \mathbf{s}_3. \end{aligned} \tag{6c} $$

Each of these matrices and vectors is presented in Appendix A. Such matrices and vectors illustrate in a very transparent way the mathematical structure of the dynamic coupling between rotating and non-rotating parts of the assembly. The coupling coefficients inside the matrices are time-dependent, varying with the angle $\phi(t)$. If the rotor operates with constant speed, the coefficients of these matrices are periodic. This kind of time-varying behaviour in the matrix coefficients introduces a parametric excitation into the system. It is important to outline that the time-varying terms in the matrices $\mathbf{M}_0$, $\mathbf{M}_1$, $\mathbf{M}_2$, $\mathbf{C}$, $\mathbf{K}_1$ and $\mathbf{K}_2$, occur in the positions corresponding to the coupling among the rotor-foundation and blades. However, the structural stiffness matrix, $\mathbf{K}_0$ is constant.

In Eqs. (6a)–(6c), it should be noted that one model contains the other, depending on the rotational speed and amplitudes of vibrations involved. For example, the second order linearized model is obtained from the linear model by including the geometric stiffness matrix, $\mathbf{K}_3$. It should be noted that this matrix $\mathbf{K}_3$ appears in both the second order linearized model and in the non-linear. Although the geometric stiffness is not explicitly included in the non-linear model, it arises from the second order non-linear terms in Eq. (5). The fully non-linear model includes also matrices and vectors which are dependent on blade displacement and velocity. Furthermore, it includes non-linear terms dependent on the square of the tip mass displacements that play an important role only when such displacements are large.

4. Theoretical and experimental results

4.1. Theoretical modal analysis

Initially, results are obtained when the rotor angular velocity is set to null. In this case, the equations of motion (6a)–(6c) are reduced to the non-rotating case, setting $\phi = \dot{\phi} = \ddot{\phi} = 0$. Such a theoretical modal analysis allows a better understanding of how the rotor-foundation motion is coupled to blade vibrations, before the rotational speed is introduced into the problem. Fig. 2 illustrates the five vibration modes of this assembly. It should be noted that the first and fifth modes present coupled motions among blades and foundation, while the second, third and fourth modes are only associated to the blade motions. The values of normalized eigenvectors are shown in Table 2. For simplicity, the first mode will be called rotor–blade mode (RB), once the horizontal motion of the rotor-foundation system is much larger than the blade motions. Modes two, three and four are blade modes (BB), once no horizontal motion of the rotor-foundation can be detected. Finally, the fifth mode represents a coupled blade–rotor mode (BR), once the blade motion is much larger than the rotor-foundation motion.

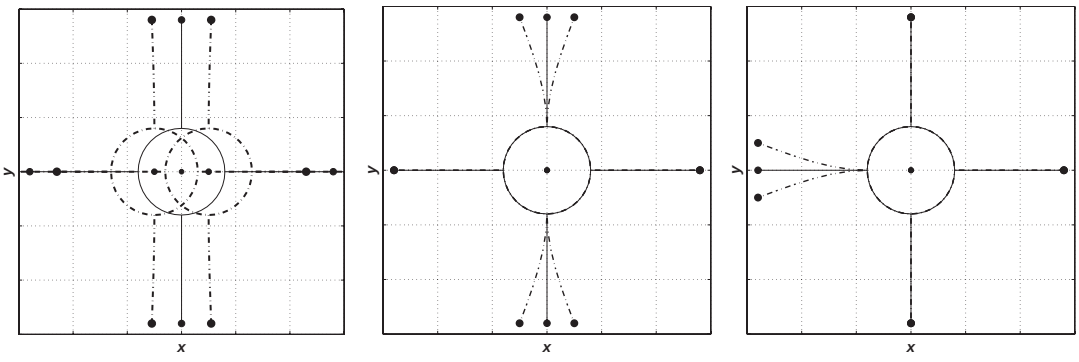

(a) Mode 1-ω_n = 6.39Hz (RB) (b) Mode 3 - ω_n = 17.35Hz (BB) (c) Mode 3 - ω_n = 17.35Hz (BB)

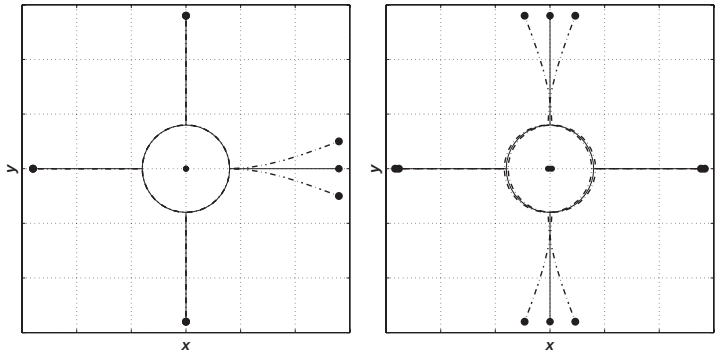

(d) Mode 4 - ω_n = 17.35Hz (BB) (e) Mode 5 - ω_n = 17.74Hz (BR)

Fig. 2. Natural mode shapes of the assembled rotor–blade system when $\dot{\phi} = 0$—numerical results.

Table 2
Non-rotating system—theoretical mode shapes

	Mode (RB)	Mode (BB)	Mode (BB)	Mode (BB)	Mode (BR)
z_0	1	0	0	0	0.071
z_1	0	0	0	1	0
z_2	−0.096	1	0	0	1
z_3	0	0	1	0	0
z_4	0.096	1	0	0	−1

The theoretical results indicate that the natural frequencies related to the blade modes (BB) and coupled blade–rotor mode (BR), according to Fig. 2, are very close to each other. Therefore, when setting up the experiment, a reasonable increment of frequency Δf should be carefully chosen, so that the different natural frequencies associated to modes (BB) and (BR) can be correctly identified. In other words, a long acquisition time is necessary in order to achieve reasonable precision in frequency domain results. In practical applications, such an increment of frequency and total acquisition time will be strongly dependent on the rotor–blade mass ratio. In this work the increment of frequency and acquisition time will be dependent on the mass relationship between rotor-foundation and tip mass.

4.2. Influence of mass ratio on the coupling modes

As noted previously, the natural frequencies related to (BB) and (BR) modes are extremely close to each other. Fig. 3 illustrates how the natural frequencies of the assembly change as a function of the mass ratio m_i/m_0, relation between the tip mass and rotor-foundation mass. The dash-dot vertical line in the plot at $m_i/m_0 = 0.0482/2.228 = 0.0216$ indicates where the mass ratio of the test rig is located. It can easily be seen that the difference between the frequencies associated with blade mode (BB) and blade–rotor coupled mode (BR) is very small, in this case. However, as the mass ratio increases the difference between the natural frequencies associated to (BB) and (BR) modes increases as well.

As the mass ratio is increased the coupling between rotor and blade co-ordinates becomes stronger, as can be seen in Figs. 4(a)–(c) for the (RB) mode and in Figs. 4(d)–(f) for the (BR) mode. When the mass ratio tends to zero, there is no coupling between rotor and blade motions. Whereas at higher mass ratio, both blade and rotor co-ordinates are highly coupled.

4.3. Waterfall diagram—parametric vibration and stiffening effect

The waterfall diagrams are created with the aim of investigating the variation of the natural frequencies and parametric vibrations of the assembly as a function of the rotational speed. Two different excitation points are used: rotor support and blade 1. The rotor is also excited by its unbalance ϵ. The responses of the rotor support and the blade 1 due to an impulsive excitation on the rotor are illustrated in Figs. 5 and 6 respectively. The response of the rotor support and the blade 1 due to an impulsive excitation on the blade 1 are illustrated in Figs. 7 and 8 respectively. In such figures the acceleration of the assembly in time domain is numerically obtained with help of the three models described by Eqs. (6a)–(6c). The mass–spring acceleration is transformed into

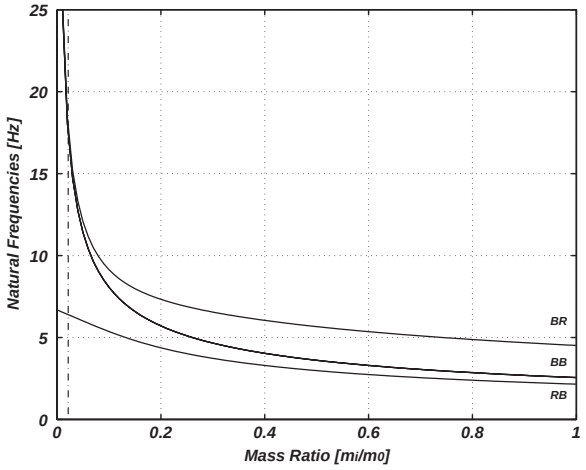

Fig. 3. Change of natural frequencies as a function of the mass ratio m_i/m_0.

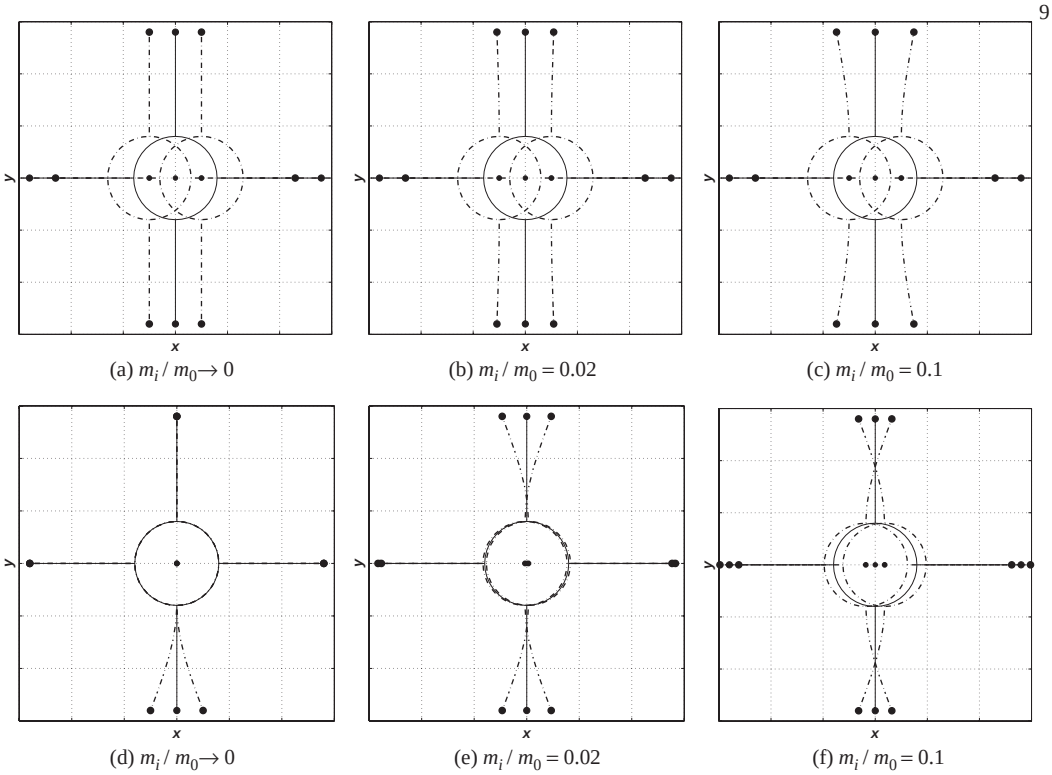

Fig. 4. Change of mode shapes (RB) and (BR) as a function of the mass ratio: (a), (b) and (c) are related to the mode (RB) and (d), (e) and (f) are related to the mode (BR).

the frequency domain by a FFT procedure. The amplitude of the FFT plots is normalized using the maximum value of the FFT-peaks at each one of the rotational speeds.

The theoretical waterfall diagrams presented in Figs. 5 and 6 clearly show the main characteristics of the system under analysis: centrifugal stiffening (increasing of the beam natural frequencies due to rotational speed) and appearance of parametric vibration, once the matrices are periodically varying with respect to the time. Parametric vibrations are vibrations whose frequency is obtained from basis-eigenvalues of the system [14–17] but added or subtracted from the changing parameter, which is, in this case, the rotational speed $\dot{\phi} = \Omega$. Figs. 5(a)–(c) show that the theoretical diagrams, obtained while exciting and measuring the foundation linear movement,

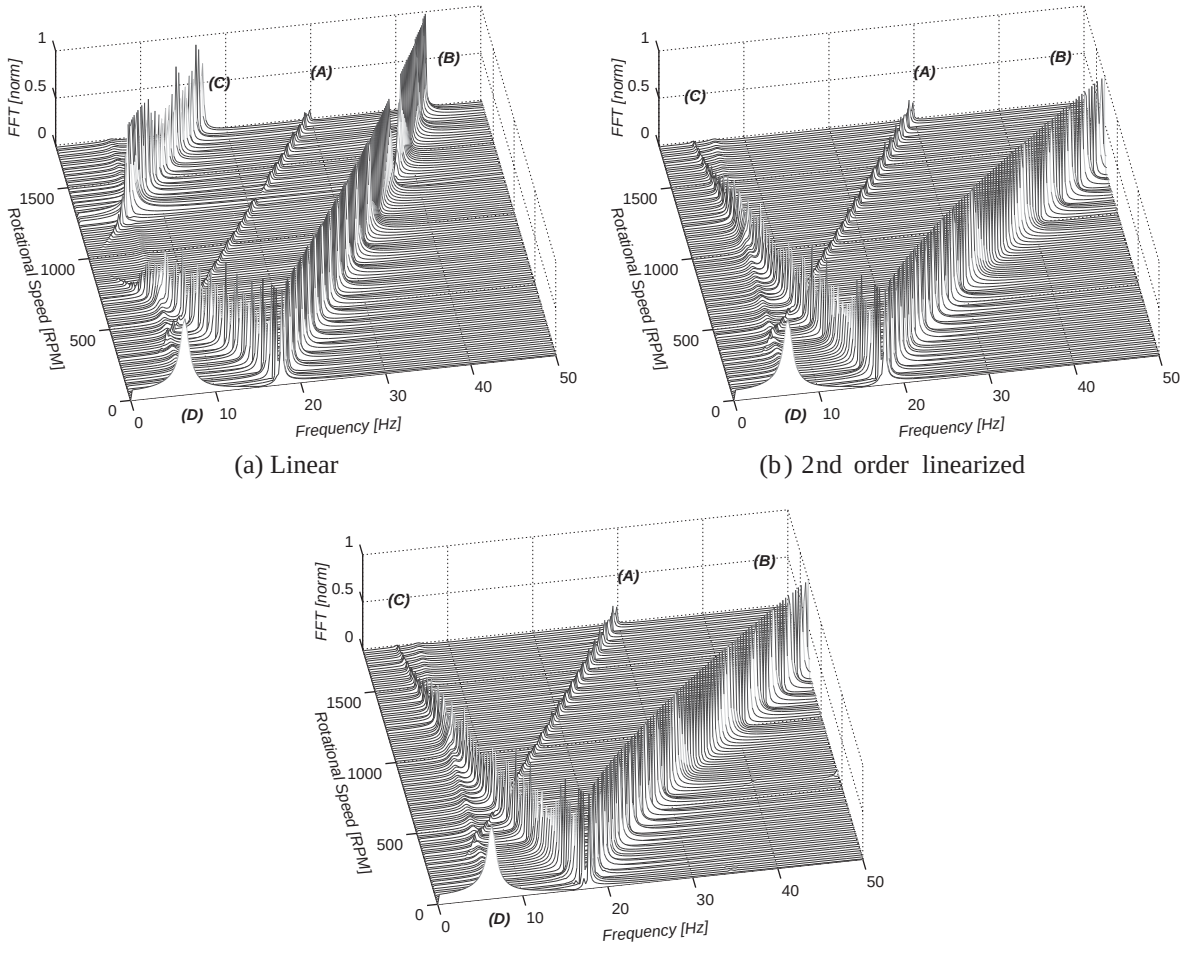

(a) Linear

(b) 2nd order linearized

(c) Fully non-linear

Fig. 5. Theoretical waterfall diagram showing the variation of the critical frequencies of the assembly as a function of the rotational speed. Excitation acting on the support mass and vibration response of the support mass on the base: (A) frequency related to the rotational speed $\dot{\phi}$; (B) frequency related to the parametric vibration of the mode (BR), $\omega_5 + \dot{\phi}$; (C) frequency related to the parametric vibration of the mode (BR), $\omega_5 - \dot{\phi}$; (D) frequency ω_1 related to the mode shape (RB), where $\omega_1 = 6.39$ Hz.

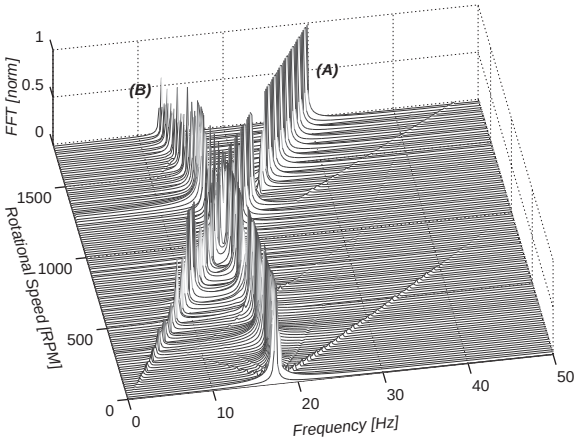

(a) Linear

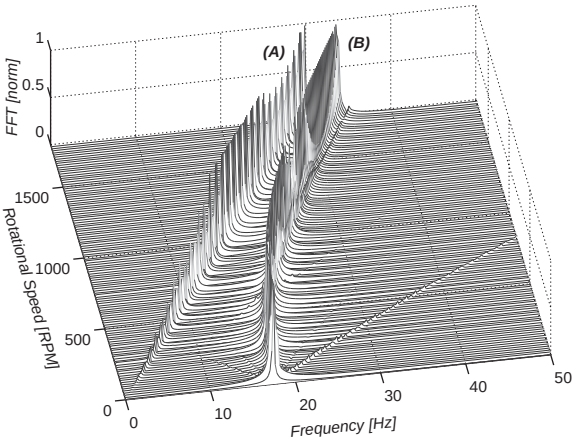

(b) 2nd order linearized

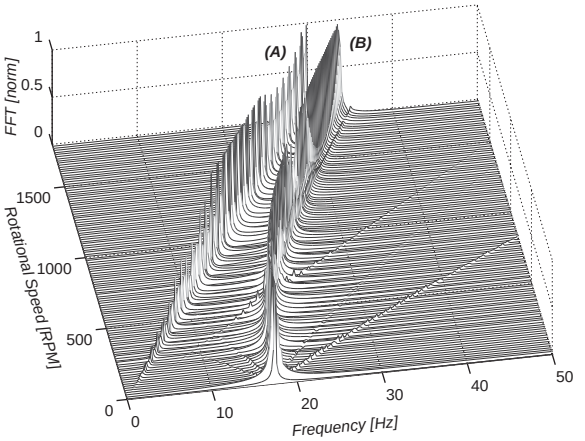

(c) Fully non-linear

Fig. 6. Theoretical waterfall diagram showing the variation of the natural frequencies of the assembly as a function of the rotational speed. Excitation acting on the support mass and vibration response of blade 1: (A) frequency related to the rotational speed $\dot{\phi}$; (B) frequency related to the blade vibrations, $\omega_2 = \omega_3 = \omega_4$, mode shape (BB).

present significant deviation among themselves. The results obtained with the linear model, Fig. 5(a) does not agree with the results obtained with the other two models in the whole range of rotational speeds. For a better understanding of Fig. 5, Figs. 6(a)–(c) have to be analyzed.

Fig. 6 illustrates the blade response (acceleration) obtained with the same excitation acting on the foundation. In this case, the behaviour of the blade natural frequency and its centrifugal stiffening are clearly observed in Figs. 6(b) and (c). Some of the peaks appearing in these diagrams of Fig. 6 are different from those appearing in Fig. 5, where the system response (acceleration) is measured at the foundation. In fact, the two peaks in Fig. 6 are related to the blade natural frequencies and to the rotational speed itself, peaks indicated by (B) and (A) respectively. Using the linear model, Eq. (6a), the natural frequency of the rotating beam lightly decreases as a

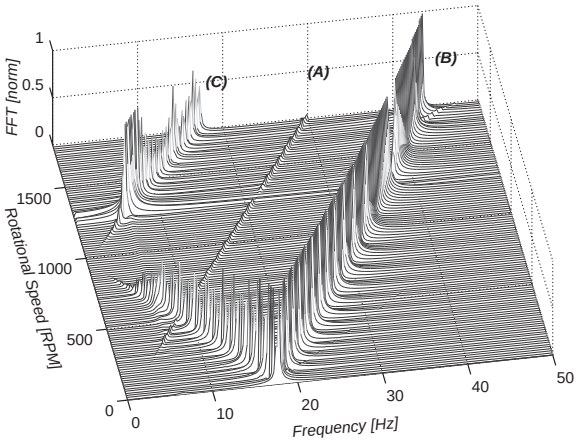

(a) Linear

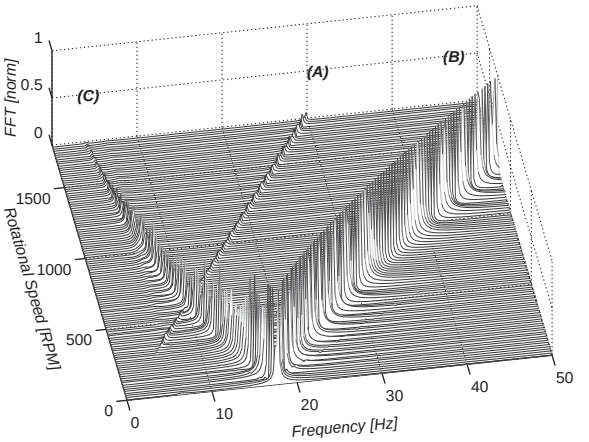

(b) 2nd order linearized

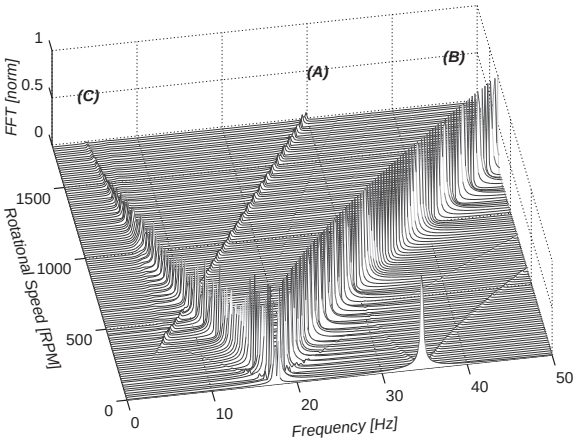

(c) Fully non-linear

Fig. 7. Theoretical waterfall diagram showing the variation of the natural frequencies of the assembly as a function of the rotational speed. Excitation acting on the blade 1 and vibration response of the support mass: (A) frequency related to the rotational speed $\dot{\phi}$; (B) frequency related to the parametric vibration of the mode (BR), $\omega_5 + \dot{\phi}$; (C) frequency related to the parametric vibration of the mode (BR), $\omega_5 - \dot{\phi}$.

function of the rotor angular velocity, see Fig. 6(a), peaks indicated by (B). Based on the second order linearized model and full non-linear model the natural frequency of the rotating beam increases as a function of the rotor angular velocity. The peaks on the right-hand side of Figs. 5(a)–(c), which open in a V-form and are indicated by (B) and (C), are related to parametric vibrations of the frequencies associated to the mode (BR). The natural frequency associated to the mode (BR) has the same behaviour as the frequency related to the mode (BB). Such parametric vibrations can only be detected while observing the linear vibrations of the support from the stationary reference frame. Vibration measurements of the assembly in the inertial and rotating reference frames will lead to peaks in different frequencies, as can be seen comparing Figs. 5

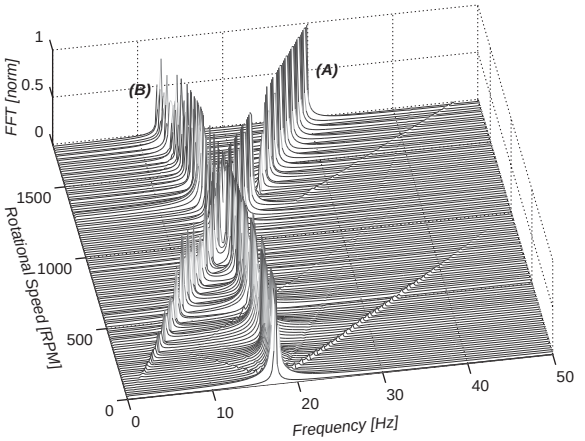

(a) Linear

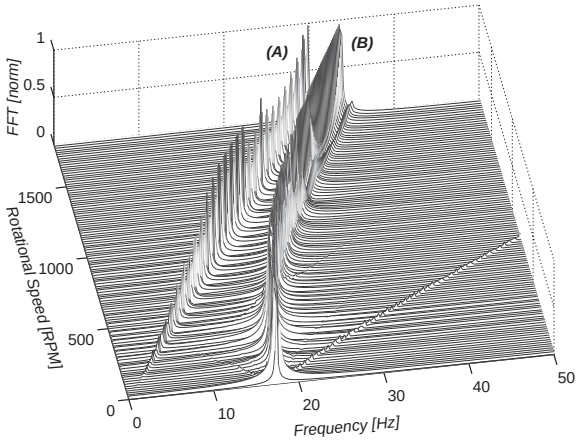

(b) 2nd order linearized

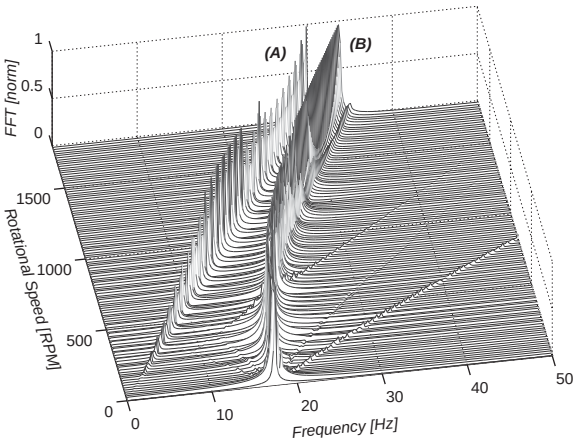

(c) Fully non-linear

Fig. 8. Theoretical waterfall diagram showing the variation of the natural frequencies of the assembly as a function of the rotational speed. Excitation acting on blade 1 and vibration response of the blade 1: (A) frequency related to the rotational speed $\dot{\phi}$; (B) frequency related to the blade vibrations, $\omega_2 = \omega_3 = \omega_4$, mode shape (BB).

and 6. The linear model predicts a reduction of the blade natural frequencies in the range of rotational speed, as can be seen in Fig. 6(a). The peak related to the parametric vibration associated to the coupled blade–rotor modes (BR), $\omega_5 - \dot{\phi}$, peaks indicated by (C) in Fig. 6, tends to null and grows again. This behaviour, obtained with help of the linear model, is completely different from those predicted by the other two models, second order linearized and fully non-linear.

In Figs. 7 and 8 the excitation is acting on one of the blades and the vibration responses are observed at the rotor-foundation (stationary reference frame) and at the blade (rotating reference frame), respectively. A similar behaviour to Figs. 5 and 6 can be seen. Discrepancies among the linear, second order linearized and fully non-linear models can be clearly seen. Comparing now

the second order linearized, Fig. 8(b) and the fully non-linear models, Fig. 8(c), significant discrepancies can be detected only for null rotor angular velocity. While exciting the assembly at one of the blades, inducing large tip mass movements, super-harmonics of the blade frequencies $\omega_2 = \omega_3 = \omega_4 = 17.34$ Hz can appear in the waterfall diagram (see peak at the frequency of $2 \times 17.34 = 34.68$ Hz in Fig. 7(c), when the rotational speed is null). Parametric vibrations associated to the super-harmonics can also be seen, but with very small amplitudes. Such effect is not obtained either using the linear nor the second order linearized model.

4.4. Experimental results

An experimental waterfall diagram is built using data from the test rig. The mass–spring system is excited by means of an impulse, generated with help of a signal generator (type 2032, B&K) and introduced into the assembly by means of the electromagnetic shaker (type 4810, B&K). The acceleration of the mass–spring system in time domain is measured using an accelerometer (type 4384, B&K) and a charge amplifier (type 2635, B&K). The acceleration signal is acquired using a PC, a digital signal processing card DT3801-G and HP-VEE software. The acquisition of the acceleration signal is triggered with help of the HP-VEE function trigger and the impulse signal. After acquiring the acceleration and impulse signals, all additional signal processing is done with help of the Matlab software. The highest frequency resolution used is $\Delta f = 0.088$ Hz. After transforming the signal into the frequency domain via FFT, it is normalized using the maximum amplitude of the FFT at each of the rotational speeds and plotted, as can be seen in Fig. 9.

When the rotor angular velocity is zero, two frequencies can be clearly recognized in the experimental waterfall diagram: $\omega_1 = 6.6$ Hz and $\omega_5 = 17.0$ Hz. The frequency associated with mode (RB), $\omega_1 = 6.6$ Hz, is not strongly influenced by the rotor angular velocity, as can be seen in the waterfall diagram, Fig. 9. The frequency related to the mode (BR), 17.0 Hz, is strongly influenced by the rotor angular velocity, as was also observed in the theoretical results.

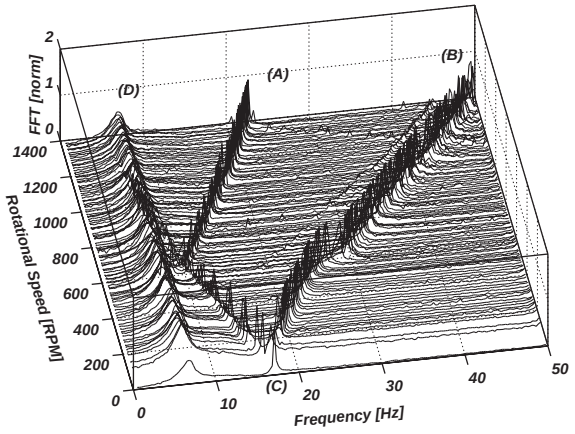

Fig. 9. Experimental waterfall diagram showing: (A) frequency related to the rotational speed $\dot{\phi}$; (B) frequency $(\omega_5 + \dot{\phi})$ related to the parametric vibration of the mode (BR); (C) frequency $(\omega_5 - \dot{\phi})$ related to the parametric vibration of the mode (BR); (D) frequency ω_1 related to the mode shape (RB), where $\omega_1 = 6.6$ Hz.

Nevertheless, with the acceleration sensor mounted directly on the support mass and excitation acting also on the support mass, only the parametric vibrations of the natural frequency ω_5, associated to the mode (BR), can be detected. Due to the stiffening effect, the frequency associated with mode (BB) increases parabolically with the rotational speed, and the frequency related to the mode (BR) follows the same behaviour. Nevertheless, in the waterfall diagram only $\omega_5 - \dot{\phi}$ and $\omega_5 + \dot{\phi}$ are detectable. The results obtained experimentally in Fig. 9 can be compared to those obtained with help of the linear model, Fig. 5(a), second order linearized, Fig. 5(b), and fully non-linear model, Fig. 5(c). One can clearly conclude that the second order linearized and fully non-linear models are able to correctly predict the stiffening effect and the parametric vibrations. The linear model can correctly estimate this behaviour only for extremely low frequencies, where the stiffening effect is of minor importance.

Table 3 shows the comparison among theoretical results, both with and without damping, and experimental ones. The experimental damping for the mode (RB) was adjusted using modal techniques [18], when the rotational speed of the assembly was set to null. Table 3 illustrates that when adding damping to the rotor-foundation system only the modes (RB) and (BR) are affected by the presence of damping. The modes (BB) associated to the blade motion are still undamped. If dissipation of blade vibration energy is aimed, dissipation mechanisms have to be attached at the rotating reference frame [19].

In Figs. 10(a) and (b) the experimental acceleration of the support mass is presented, when an impulsive excitation acts on the support mass and on blade 1 respectively. The results are presented in time as well as in frequency domains, and show beating and non-linear effects (super-harmonics due to blade vibrations with large amplitudes). The fundamental frequency is 16.5 Hz. This frequency is associated to the modes (BB), where $\omega_2 = \omega_3 = \omega_4 = 16.5$ Hz, see Fig. 2. Its

Table 3
Non-rotating system—theoretical and experimental frequencies

	Mode 1 (RB)	Mode 2 (BB)	Mode 3 (BB)	Mode 4 (BB)	Mode 5 (BR)
Theo. (Hz)	6.39	17.34	17.34	17.34	17.73
Exp. (Hz)	6.60	16.5	16.5	16.5	17.0
Diff. (%)	3.18	5.09	5.09	5.09	4.29
No damping					
z_0	1	0	0	0	0.0716
z_1	0	0	0	1	0
z_2	−0.0960	1	0	0	1
z_3	0	0	1	0	0
z_4	0.0960	1	0	0	−1
Damping at foundation $d_o = 13.1$ N m/s					
z_0	0.9979−0.0021i	0	0	0	0.0714 + 0.0040i
z_1	0	0	0	1	0
z_2	−0.0945−0.0145i	1	0	0	1
z_3	0	0	1	0	0
z_4	0.0945 + 0.0145i	1	0	0	−1

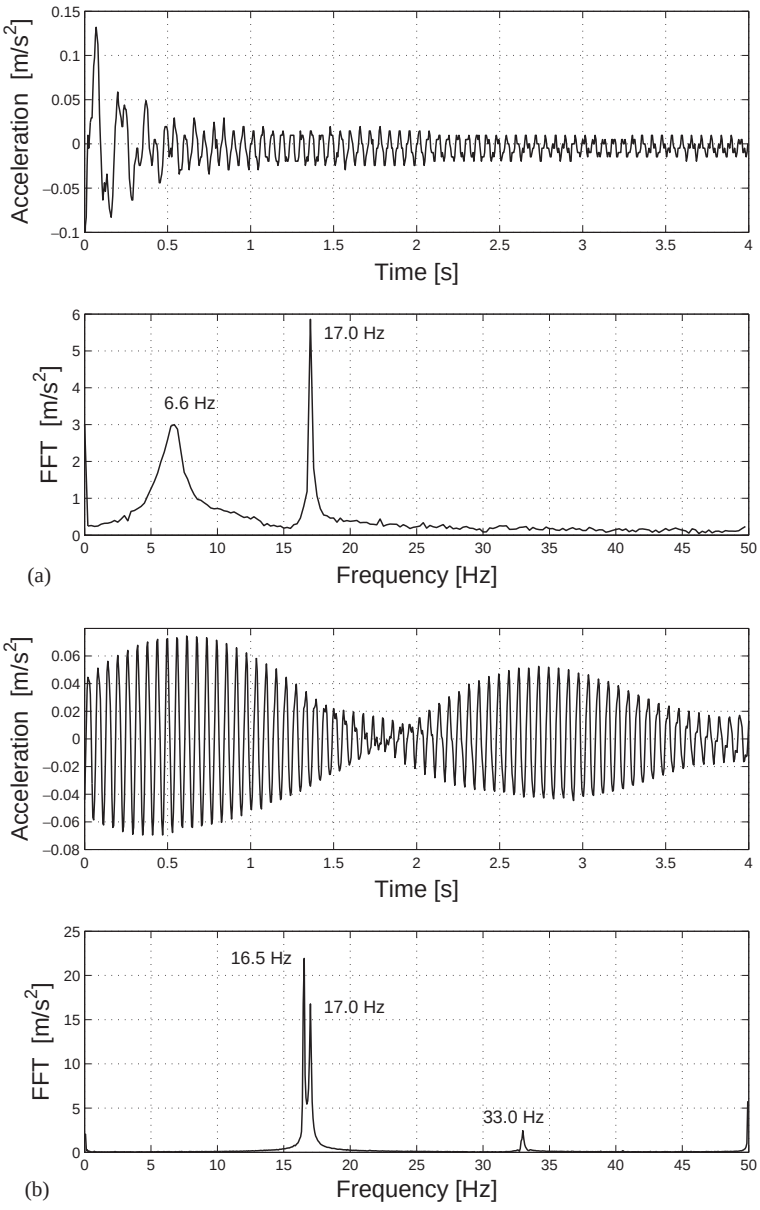

Fig. 10. Experimental acceleration of the support mass due to an impulsive excitation acting: (a) on the support mass; (b) on one of the blades—rotor angular velocity is null.

super-harmonic component, $2 \times \omega_2 = 33.0$ Hz, can be experimentally detected in Fig. 10(b), and also predicted by the fully non-linear model, see Fig. 8(c). The natural frequency associated to the mode (BR) is $\omega_5 = 17.0$ Hz. When the blade is excited, strong blade-structure coupled vibrations are detected, as can be seen in Fig. 10(b) in time domain. The beating is resulting from the small

difference between the natural frequencies related to the modes (BB) and (BR), 16.5 and 17.0 Hz respectively.

5. Conclusion

Comparing the results coming from the three different mathematical models to the experimental ones, the second order linearized and fully non-linear models are those which can correctly predict the stiffening effect and coupled parametric vibrations of the rotor–blade assembly. The linear model can correctly estimate parametric vibrations only in a short range of low rotational speed, where the stiffening effect is of minor importance. Super-harmonic vibration associated to the movement of the flexible rotating parts (with large amplitude) can only be detected with the help of the fully non-linear model.

From the viewpoint of vibration monitoring in rotating flexible structures one can conclude that the positioning of sensors at stationary or rotating reference frames will lead to peaks in different frequencies. With sensors attached to the non-rotating part of the structure (inertial reference frame) one will detect parametric vibrations related to the coupled mode shapes of the flexible rotating parts and flexible non-rotating parts.

In rotor–bearing systems coupled to flexible blades, the lighter the flexible blades are, the closer are the modes (BB) and (BR). It means that a long acquisition time is necessary in order to achieve a reasonable precision in the frequency domain and correctly identify both frequencies and modes.

Acknowledgements

The authors are grateful to the Fundação de Amparo à Pesquisa do Estado de São Paulo—FAPESP—for the financial support.

Appendix A. Matrices and vectors

$$\mathbf{M}_0 = \begin{bmatrix} m_0 + \sum_{i=1}^{p=4} m_i & & & & \text{Sym} \\ -\frac{m_1(2L_1+3rt_1)}{2L_1}\sin(\phi+\theta_1) & \frac{9It_1+m_1(2L_1+3rt_1)^2}{4L_1^2} & & & \\ -\frac{m_2(2L_2+3rt_2)}{2L_2}\sin(\phi+\theta_2) & 0 & \frac{9It_2+m_2(2L_2+3rt_2)^2}{4L_2^2} & & \\ -\frac{m_3(2L_3+3rt_3)}{2L_3}\sin(\phi+\theta_3) & 0 & 0 & \frac{9It_3+m_3(2L_3+3rt_3)^2}{4L_3^2} & \\ -\frac{m_4(2L_4+3rt_4)}{2L_4}\sin(\phi+\theta_4) & 0 & 0 & 0 & \frac{9It_4+m_4(2L_4+3rt_4)^2}{4L_4^2} \end{bmatrix}, \tag{A.1}$$

$$\mathbf{M}_1 = \begin{bmatrix} 0 & & & & \text{Sym} \\ -\frac{9m_1rt_1}{4L_1^2} z_1 \cos(\phi+\theta_1) & 0 & & & \\ -\frac{9m_2rt_2}{4L_2^2} z_2 \cos(\phi+\theta_2) & 0 & 0 & & \\ -\frac{9m_3rt_3}{4L_3^2} z_3 \cos(\phi+\theta_3) & 0 & 0 & 0 & \\ -\frac{9m_4rt_4}{4L_4^2} z_4 \cos(\phi+\theta_4) & 0 & 0 & 0 & 0 \end{bmatrix}$$

$$+ \begin{bmatrix} 0 & & & & \text{Sym} \\ -\frac{6m_1}{5L_1} z_1 \cos(\phi+\theta_1) & 0 & & & \\ -\frac{6m_2}{5L_2} z_2 \cos(\phi+\theta_2) & 0 & 0 & & \\ -\frac{6m_3}{5L_3} z_3 \cos(\phi+\theta_3) & 0 & 0 & 0 & \\ -\frac{6m_4}{5L_4} z_4 \cos(\phi+\theta_4) & 0 & 0 & 0 & 0 \end{bmatrix}, \tag{A.2}$$

$$\mathbf{M}_2 = \begin{bmatrix} 0 & & & & \text{Sym} \\ \frac{27m_1rt_1}{16L_1^3} z_1^2 \sin(\phi+\theta_1) & -\frac{27m_1rt_1}{8L_1^3} z_1^2 & & & \\ \frac{27m_2rt_2}{16L_2^3} z_2^2 \sin(\phi+\theta_2) & 0 & -\frac{27m_2rt_2}{8L_2^3} z_2^2 & & \\ \frac{27m_3rt_3}{16L_3^3} z_3^2 \sin(\phi+\theta_3) & 0 & 0 & -\frac{27m_3rt_3}{8L_3^3} z_3^2 & \\ \frac{27m_4rt_4}{16L_4^3} z_4^2 \sin(\phi+\theta_4) & 0 & 0 & 0 & -\frac{27m_4rt_4}{8L_4^3} z_4^2 \end{bmatrix}$$

$$+ \begin{bmatrix} 0 & & & & \text{Sym} \\ 0 & \frac{(36L_1+135rt_1)m_1}{25L_1^3} z_1^2 & & & \\ 0 & 0 & \frac{(36L_2+135rt_2)m_2}{25L_2^3} z_2^2 & & \\ 0 & 0 & 0 & \frac{(36L_3+135rt_3)m_3}{25L_3^3} z_3^2 & \\ 0 & 0 & 0 & 0 & \frac{(36L_4+135rt_4)m_4}{25L_4^3} z_4^2 \end{bmatrix}, \tag{A.3}$$

$$\mathbf{K}_0 = \begin{bmatrix} k_0 & 0 & 0 & 0 & 0 \\ 0 & k_1 & 0 & 0 & 0 \\ 0 & 0 & k_2 & 0 & 0 \\ 0 & 0 & 0 & k_3 & 0 \\ 0 & 0 & 0 & 0 & k_4 \end{bmatrix}, \tag{A.4}$$

$$\mathbf{K}_{p_1} = g\begin{bmatrix} 0 & 0 & 0 & 0 & 0 \\ 0 & -m_1\frac{6\sin(\theta_1+\phi)}{5L_1} & 0 & 0 & 0 \\ 0 & 0 & -m_2\frac{6\sin(\theta_2+\phi)}{5L_2} & 0 & 0 \\ 0 & 0 & 0 & -m_3\frac{6\sin(\theta_3+\phi)}{5L_3} & 0 \\ 0 & 0 & 0 & 0 & -m_4\frac{6\sin(\theta_4+\phi)}{5L_4} \end{bmatrix} \tag{A.5}$$

$$\mathbf{K}_{p_2} = g\begin{bmatrix} 0 & 0 & 0 & 0 & 0 \\ 0 & -\frac{9rt_1}{4L_1^2}\sin(\phi+\theta_1) & 0 & 0 & 0 \\ 0 & 0 & -\frac{9rt_2}{4L_2^2}\sin(\phi+\theta_2) & 0 & 0 \\ 0 & 0 & 0 & -\frac{9rt_3}{4L_3^2}\sin(\phi+\theta_3) & 0 \\ 0 & 0 & 0 & 0 & -\frac{9rt_4}{4L_4^2}\sin(\phi+\theta_4) \end{bmatrix}, \tag{A.6}$$

$$\mathbf{K}_1 = \dot{\phi}^2\begin{bmatrix} 0 & \frac{m_1(2L_1+3rt_1)}{2L_1}\sin(\phi+\theta_1) & \frac{m_2(2L_2+3rt_2)}{2L_2}\sin(\phi+\theta_2) & \frac{m_3(2L_3+3rt_3)}{2L_3}\sin(\phi+\theta_3) & \frac{m_4(2L_4+3rt_4)}{2L_4}\sin(\phi+\theta_4) \\ 0 & -\frac{4L_1^2+3rt_1(L_1-3rt_1)}{4L_1^2}m_1 & 0 & 0 & 0 \\ 0 & 0 & -\frac{4L_2^2+3rt_2(L_2-3rt_2)}{4L_2^2}m_2 & 0 & 0 \\ 0 & 0 & 0 & -\frac{4L_3^2+3rt_3(L_3-3rt_3)}{4L_3^2}m_3 & 0 \\ 0 & 0 & 0 & 0 & -\frac{4L_4^2+3rt_4(L_4-3rt_4)}{4L_4^2}m_4 \end{bmatrix}, \tag{A.7}$$

$$\mathbf{K}_2 = \ddot{\phi}\begin{bmatrix} 0 & -\frac{m_1(2L_1+3rt_1)}{2L_1}\cos(\phi+\theta_1) & -\frac{m_2(2L_2+3rt_2)}{2L_2}\cos(\phi+\theta_2) & -\frac{m_3(2L_3+3rt_3)}{2L_3}\cos(\phi+\theta_3) & -\frac{m_4(2L_4+3rt_4)}{2L_4}\cos(\phi+\theta_4) \\ 0 & 0 & 0 & 0 & 0 \\ 0 & 0 & 0 & 0 & 0 \\ 0 & 0 & 0 & 0 & 0 \\ 0 & 0 & 0 & 0 & 0 \end{bmatrix}, \tag{A.8}$$

$$\mathbf{K}_3 = \dot{\phi}^2\begin{bmatrix} 0 & 0 & 0 & 0 & 0 \\ 0 & m_1\frac{6(L_1+r_1+rt_1)}{5L_1} & 0 & 0 & 0 \\ 0 & 0 & m_2\frac{6(L_2+r_2+rt_2)}{5L_2} & 0 & 0 \\ 0 & 0 & 0 & m_3\frac{6(L_3+r_3+rt_3)}{5L_3} & 0 \\ 0 & 0 & 0 & 0 & m_4\frac{6(L_4+r_4+rt_4)}{5L_4} \end{bmatrix}, \tag{A.9}$$

$$\mathbf{C} = \dot{\phi}\begin{bmatrix} 0 & -\frac{m_1(2L_1+3rt_1)}{L_1}\cos(\phi+\theta_1) & -\frac{m_2(2L_2+3rt_2)}{L_2}\cos(\phi+\theta_2) & -\frac{m_3(2L_3+3rt_3)}{L_3}\cos(\phi+\theta_3) & -\frac{m_4(2L_4+3rt_4)}{L_4}\cos(\phi+\theta_4) \\ 0 & 0 & 0 & 0 & 0 \\ 0 & 0 & 0 & 0 & 0 \\ 0 & 0 & 0 & 0 & 0 \\ 0 & 0 & 0 & 0 & 0 \end{bmatrix}, \tag{A.10}$$

$$\mathbf{f}_p = -g\begin{Bmatrix} 0 \\ m_1\frac{2L_1+3rt_1}{2L_1}\cos(\phi+\theta_1) \\ m_2\frac{2L_2+3rt_2}{2L_2}\cos(\phi+\theta_2) \\ m_3\frac{2L_3+3rt_3}{2L_3}\cos(\phi+\theta_3) \\ m_4\frac{2L_4+3rt_4}{2L_4}\cos(\phi+\theta_4) \end{Bmatrix}, \tag{A.11}$$

$$\mathbf{f}_1 = \dot{\phi}^2\begin{Bmatrix} \varepsilon m_0\cos(\phi+\varphi) + \sum_{i=1}^{p=4} m_i(L_i+r_i+rt_i)\cos(\phi+\theta_i) \\ 0 \\ 0 \\ 0 \\ 0 \end{Bmatrix}, \tag{A.12}$$

$$\mathbf{f}_2 = \ddot{\phi}\begin{Bmatrix} \varepsilon m_0\sin(\phi+\varphi) + \sum_{i=1}^{p=4} m_i(L_i+r_i+rt_i)\sin(\phi+\theta_i) \\ -\frac{3It_1+m_1(L_1+r_1+rt_1)(2L_1+3rt_1)}{2L_1} \\ -\frac{3It_2+m_2(L_2+r_2+rt_2)(2L_2+3rt_2)}{2L_2} \\ -\frac{3It_3+m_3(L_3+r_3+rt_3)(2L_3+3rt_3)}{2L_3} \\ -\frac{3It_4+m_4(L_4+r_4+rt_4)(2L_4+3rt_4)}{2L_4} \end{Bmatrix}, \tag{A.13}$$

$$\mathbf{s}_0 = \begin{Bmatrix} \sum_{i=1}^{p=4} \frac{9m_irt_i}{4L_i^2}\dot{z}_i^2\cos(\phi+\theta_i) - \frac{27m_irt_i}{8L_i^3}z_i\dot{z}_i^2\sin(\phi+\theta_i) + \frac{81m_irt_i}{32L_i^4}z_i^2\dot{z}_i^2\cos(\phi+\theta_i) \\ \frac{27m_1rt_1g}{16L_1^3}\cos(\phi+\theta_1)z_1^2 + \frac{27m_1rt_1}{8L_1^3}z_1\dot{z}_1^2 \\ \frac{27m_2rt_2g}{16L_2^3}\cos(\phi+\theta_2)z_2^2 + \frac{27m_2rt_2}{8L_2^3}z_2\dot{z}_2^2 \\ \frac{27m_3rt_3g}{16L_3^3}\cos(\phi+\theta_3)z_3^2 + \frac{27m_3rt_3}{8L_3^3}z_3\dot{z}_3^2 \\ \frac{27m_4rt_4g}{16L_4^3}\cos(\phi+\theta_4)z_4^2 + \frac{27m_4rt_4}{8L_4^3}z_4\dot{z}_4^2 \end{Bmatrix}$$

$$+\begin{Bmatrix} \sum_{i=1}^{p=4} \frac{6m_i}{5L_i}\dot{z}_i^2\cos(\phi+\theta_i) \\ -\frac{36mp_1}{25L_1^2}z_1\dot{z}_1^2-\frac{27m_1rt_1g}{5L_1^3}z_1\dot{z}_1^2+\frac{243m_1rt_1}{80L_1^5}z_1^3\dot{z}_1^2 \\ -\frac{36mp_2}{25L_2^2}z_2\dot{z}_2^2-\frac{27m_2rt_2g}{5L_2^3}z_2\dot{z}_2^2+\frac{243m_2rt_2}{80L_2^5}z_2^3\dot{z}_2^2 \\ -\frac{36mp_3}{25L_3^2}z_3\dot{z}_3^2-\frac{27m_3rt_3g}{5L_3^3}z_3\dot{z}_3^2+\frac{243m_3rt_3}{80L_3^5}z_3^3\dot{z}_3^2 \\ -\frac{36mp_4}{25L_4^2}z_4\dot{z}_4^2-\frac{27m_4rt_4g}{5L_4^3}z_4\dot{z}_4^2+\frac{243m_4rt_4}{80L_4^5}z_4^3\dot{z}_4^2 \end{Bmatrix}, \tag{A.14}$$

$$\mathbf{s}_1=\ddot{\phi}\begin{Bmatrix} -\frac{9}{8}\sum_{i=1}^{p=4}\frac{m_irt_i}{L_i^2}z_i^2\sin(\phi+\theta_i) \\ \frac{9m_1(L_1+3r_1)rt_1}{16L_1^3}z_1^2 \\ \frac{9m_2(L_2+3r_2)rt_2}{16L_2^3}z_2^2 \\ \frac{9m_3(L_3+3r_3)rt_3}{16L_3^3}z_3^2 \\ \frac{9m_4(L_4+3r_4)rt_4}{16L_4^3}z_4^2 \end{Bmatrix}+\ddot{\phi}\begin{Bmatrix} -\frac{3}{5}\sum_{i=1}^{p=4}\frac{m_i}{L_i}z_i^2\sin(\phi+\theta_i) \\ -\frac{3m_1}{5L_1}z_1^2-\frac{9m_1rt_1}{10L_1}z_1^2-\frac{81m_1rt_1}{80L_1}z_1^4 \\ -\frac{3m_2}{5L_2}z_2^2-\frac{9m_2rt_2}{10L_2}z_2^2-\frac{81m_2rt_2}{80L_2}z_2^4 \\ -\frac{3m_3}{5L_3}z_3^2-\frac{9m_3rt_3}{10L_3}z_3^2-\frac{81m_3rt_3}{80L_3}z_3^4 \\ -\frac{3m_4}{5L_4}z_4^2-\frac{9m_4rt_4}{10L_4}z_4^2-\frac{81m_4rt_4}{80L_4}z_4^4 \end{Bmatrix}, \tag{A.15}$$

$$\mathbf{s}_2=\dot{\phi}^2\begin{Bmatrix} -\frac{9}{8}\sum_{i=1}^{p=4}\frac{m_irt_i}{L_i^2}z_i^2\cos(\phi+\theta_i) \\ -\frac{27m_1rt_1}{16L_1^3}z_1^3 \\ -\frac{27m_2rt_2}{16L_2^3}z_2^3 \\ -\frac{27m_3rt_3}{16L_3^3}z_3^3 \\ -\frac{27m_4rt_4}{16L_4^3}z_4^3 \end{Bmatrix}+\dot{\phi}^2\begin{Bmatrix} -\frac{3}{5}\sum_{i=1}^{p=4}\frac{m_i}{L_i}z_i^2\cos(\phi+\theta_i) \\ \frac{18m_1}{25L_1^2}z_1^3+\frac{81m_1rt_1}{80L_1^3}z_1^3 \\ \frac{18m_2}{25L_2^2}z_2^3+\frac{81m_2rt_2}{80L_2^3}z_2^3 \\ \frac{18m_3}{25L_3^2}z_3^3+\frac{81m_3rt_3}{80L_3^3}z_3^3 \\ \frac{18m_4}{25L_4^2}z_4^3+\frac{81m_4rt_4}{80L_4^3}z_4^3 \end{Bmatrix}, \tag{A.16}$$

$$\mathbf{s}_3=\dot{\phi}\begin{Bmatrix} -\frac{9}{8}\sum_{i=1}^{p=4}\frac{4m_irt_i}{L_i^2}z_i\dot{z}_i\sin(\phi+\theta_i)+\frac{3m_irt_i}{L_i^3}z_i^2\dot{z}_i\cos(\phi+\theta_i) \\ 0 \\ 0 \\ 0 \\ 0 \end{Bmatrix}$$

$$+\dot{\phi}\begin{Bmatrix} -\frac{12}{5}\sum_{i=1}^{p=4}\frac{m_i}{L_i}z_i\dot{z}_i\sin(\phi+\theta_i) \\ 0 \\ 0 \\ 0 \\ 0 \end{Bmatrix}. \tag{A.17}$$

References

[1] G.L. Anderson, On the extensional and flexural vibrations of rotating bars, *International Journal of Non-Linear Mechanics* 10 (1975) 223–236.
[2] J.C. Simo, L. Vu-Quoc, The role of non-linear theories in transient dynamic analysis of flexible structures, *Journal of Sound and Vibration* 119 (3) (1987) 487–508.
[3] H. Baruh, *Analytical Dynamics*, McGraw-Hill, New York, 1998.
[4] E.M. Bakr, A.A. Shabana, Geometrically nonlinear analysis of a multibody systems, *Computers and Structures* 23 (6) (1986) 739–751.
[5] J. Mayo, J. Domínguez, Geometrically non-linear formulation of flexible multibody systems in terms of beam elements: geometric stiffness, *Computers & Structures* 59 (6) (1996) 1039–1050.
[6] J. Mayo, J. Domínguez, A.A. Shabana, Geometrically nonlinear formulations of beams in flexible multibody dynamics, *Journal of Vibration and Acoustics* 117 (4) (1995) 501–509.
[7] M.P. Cartmell, The equation of motion for a parametrically excited cantilever beam, *Journal of Vibration and Acoustics* 143 (3) (1990) 395–406.
[8] D.M.I. Forehand, M.P. Cartmell, On the derivation of the equation of motion for a parametrically excited cantilever beam, *Journal of Vibration and Acoustics* 245 (1) (2001) 165–177.
[9] H. Bremer, *Dynamik und Regelung Mechanischer Systeme*, Teubner, Stuttgart, 1988.
[10] A. Yigit, R.A. Scott, A.G. Ulsoy, Flexural motion of a radially rotating beam attached to a rigid body, *Journal of Sound and Vibration* 121 (2) (1988) 201–220.
[11] B. Fallahi, S.H.-Y. Lai, An improved numerical scheme for characterizing dynamic behaviour of high-speed rotating elastic beam structures, *Computers & Structures* 50 (6) (1994) 749–755.
[12] C.M. Saracho, I.F. Santos, Dynamic models for coupled blade–rotor vibrations, *Proceedings of IX Diname*, *International Conference on Dynamic Problems in Mechanics*, Florianopolis, Brazil, 5–9 March 2001, pp. 263–268.
[13] V. Radisavljevic, H. Baruh, A comparison of shortening of the projection to axial deformation. *Proceedings of the 42nd AIAA/ASME/ASCE/AHS/ASC Structures*, *Structural Dynamics*, *and Materials Conference*, Seattle, WA, 16–19 April 2001 (CD-ROM), pp. 1–9.
[14] M. Wiedemann, R. Gasch, Rotor–Blatt–Kopplung, *Archive of Applied Mechanics* 63 (1993) 337–344.
[15] J. Xu, R. Gasch, Modale Behandlung linear periodisch zeitvarianter Bewegungsgleichungen, *Archive of Applied Mechanics* 65 (1995) 178–193.
[16] H. Irretier, Mathematical foundations of experimental modal analysis in rotor dynamics, *Mechanical Systems and Signal Processing* 13 (1999) 183–191.
[17] I. Bucher, D.J. Ewins, Modal analysis and testing of rotating structures, *Philosophical Transactions of the Royal Society of London* 359 (2001) 61–96.
[18] D.J. Ewins, *Modal Testing: Theory and Practice*, Research Studies Press Ltd., Taunton, 1984.
[19] M. Hajek, Reibungsdämper für Turbinenschaufeln, vol. 128, Fortschrittberichte VDI, Reihe 11, Schwingungstechnik, VDI-Verlag, Dusseldorf, 1990.